Author manuscript, published in "Geophysical Journal International 174, 2 (2008) 489-504"
DOI : 10.1111/j.1365-246X.2008.03828.x

Evidence of the theoretically predicted seismo-magnetic conversion

Clarisse Bordes

Modélisation et Imagerie en Géosciences, Avenue de l'Université (UMR 5212),

64000 Pau, France

clarisse.bordes@univ-pau.fr

and

Laboratoire de Géophysique Interne et Tectonophysique (UMR 5559),

1381 rue de la Piscine, 38041 Grenoble Cedex 9, France

Laurence Jouniaux

Institut de Physique du Globe de Strasbourg (UMR 7516),

5 rue R. Descartes, 67084 Strasbourg

Laurence.Jouniaux@eost.u-strasbg.fr

Stéphane Garambois

Laboratoire de Géophysique Interne et Tectonophysique (UMR 5559),

1391 rue de la Piscine, 38041 Grenoble Cedex 9, France

Stéphane.Garambois@ujf-grenoble.fr

Michel Dietrich

Laboratoire de Géophysique Interne et Tectonophysique (UMR 5559),

1391 rue de la Piscine, 38041 Grenoble Cedex 9, France

Michel.Dietrich@ujf-grenoble.fr

Jean-Pierre Pozzi

Ecole Normale Supérieure (UMR 8538), 24 Rue Lhomond, 75231 Paris Cedex 05

pozzi@geologie.ens.fr

Stéphane Gaffet

Laboratoire Géosciences Azur (UMR 6526),

250 rue Albert Einstein, Sophia Antipolis 06560 Valbonne, France

gaffet@geoazur.unice.fr

Abstract

Seismo-electromagnetic phenomena in porous media arise from seismic wave-induced fluid motion in the pore space, which perturbs the equilibrium of the electric double layer. This paper describes with details the original experimental apparatus built within the ultra-shielded chamber of the Low Noise Underground Laboratory of Rustrel (France). We measured seismo-magnetic conversions in moist sand using two induction magnetometers, and a pneumatic seismic source to generate the seismic wave propagation. We ensured to avoid the magnetometer vibrations, which could induce strong disturbances from induction origin. Interpretation of the data is improved by an analytical description of phase velocities for fast (P_f) and slow (P_s) longitudinal modes, transverse mode (S) as well as the extensional mode due to the cylindrical geometry of the sample.

The purpose of this paper is to provide elements to measure correctly co-seismic seismomagnetic fields and to specify their amplitude. The seismic arrivals recorded in the sample showing a 1200-1300 $m.s^{-1}$ velocity have been associated to P and extensional waves. The measured seismo-magnetic arrivals show a velocity of about 800 $m.s^{-1}$ close to the calculated phase velocity of S waves. Therefore we show that the seismo-magnetic field is associated to the transverse part of the propagation, as theoretically predicted by Pride (1994), but never measured up to now. Moreover, the combined experimental and analytical approaches lead us to the conclusion that the measured seismo-magnetic field is probably about 0.035 nT for a 1 $m.s^{-2}$ seismic source acceleration (0.1 g).

1 Introduction

Seismic wave propagation in fluid-filled porous media generates electromagnetic phenomena due to electrokinetic couplings at the pore scale. These conversions are due to the relative motions of electrolyte ions with respect to the mineral surface (grains). Origin of these phenomena is generally attributed to an electrical double (Overbeek, 1952) or triple-layer (Davis et al., 1978) at the rock/electrolyte interface. As a consequence, seismic wave propagation in the porous media can be accompanied by transient electric and magnetic fields created in the homogeneous porous medium. Existing investigations of the seismo-electromagnetic effects account for two main kinds of electrokinetic conversions:

1. In a homogeneous media, the pore fluid dragging ions of the electrolyte causes an electrical convection current. This current is naturally balanced by an equal and opposite conduction current that establishes an electrical potential gradient. Under an oscillating pressure source, the potential will linearly change in amplitude and sign with the pressure. This electrical potential will be seen as a wave travelling with the pressure, but since the total current is zero, no electric nor magnetic field will be observed outside the area of disturbances. This phenomena is the coseismic part of the seismo-electromagnetic phenomena.

2. On the other hand, when the seismic wave crosses an interface, an electrical current imbalance can be induced by the contrast of porous media properties (Garambois et al., 2002). This acts as the source for an electromagnetic disturbance, traveling with high speed and spreading throughout the formation.

Seismo-electromagnetic effects are especially appealing for environmental or oil exploration as they open the possibility to characterize the fluids contained in the subsurface or in reservoir rocks with the resolution of seismic methods. The second kind of seismo-electromagnetic conversion occurs at a contrast in electrical impedance, even if there is no contrast in seismic impedance. Interfaces

between permeable or fractured zones may be detected by the measurement of either seismic to electric conversion (Thompson & Gist, 1993) or electric to seismic conversion (Thompson et al., 2005). However, since the induced signals are low-amplitude signals, this method may not be efficient to characterize very deep formations, except in boreholes or using very high powerful seismic sources.

Over the past decades, field experiments were conducted to characterize these seismo-electromagnetic phenomena (Thompson, 1936; Martner & Sparks, 1959; Broding et al., 1963; Long & Rivers, 1975). Successful field experiments performed in recent years (Butler & Russell, 1993; Thompson & Gist, 1993; Russell et al., 1997; Mikhailenko & Soboleva, 1997; Beamish, 1999; Hunt & Worthington, 2000; Garambois & Dietrich, 2001; Kepic & Rosid, 2004; Thompson et al., 2005; Dupuis & Butler, 2006; Haines et al., 2007a,b; Dupuis et al., 2007; Strahser et al., 2007) have stimulated new interest in this particular mechanism. As described by Pride (1994), analytical interpretation of these phenomena needs to connect the theory of Biot (1956) for the seismic wave propagation in a two phases medium with the Maxwell's equations, using dynamic electrokinetic couplings. These analytical developments opened the possibility to numerically simulate the electrokinetic coupling phenomena in homogeneous or layered saturated media (Haartsen & Pride, 1997; Haartsen et al., 1998; Singer & Fainberg, 1999; Garambois & Dietrich, 2001, 2002) with applications to reservoir geophysics (Hu & Wang, 2000; Singer et al., 2005; Jackson et al., 2005; Saunders et al., 2006).

Some laboratory studies exist on the zero-frequency limit, often referred to as the streaming potential (Ishido & Mizutani, 1981; Pozzi & Jouniaux, 1994; Jouniaux & Pozzi, 1995a,b, 1997; Pengra et al., 1999; Lorne et al., 1999a,b; Jouniaux et al., 2000; Doussan et al., 2002; Hase et al., 2003; Guichet et al., 2003, 2006). Applying a sinusoidal fluid pressure, some authors studied the frequency-dependence of the streaming potential (Packard, 1953; Cooke, 1955; Reppert et al., 2001). These measurements on sand or core samples showed that the electrokinetic effect is particularly sensitive to the fluid conductivity, to the fluid-pH, and to the water-saturation state. However, few labora-

tory experiments have been performed on dynamic seismo-electric conversions (Parkhomenko & Tsze-San, 1964; Gaskarov & Parkhomenko, 1974; Chandler, 1981; Mironov et al., 1994; Jiang et al., 1998; Ageeva et al., 1999; Zhu et al., 2000) some of them focusing on laboratory borehole measurements (Zhu et al., 1999; Zhu & Toksöz, 2003, 2005). Recently Chen & Mu (2005) as well as Block & Harris (2006) confirmed that a seismic wave crossing an interface induces an electromagnetic field, with electrokinetic origin, by measuring the associated electric field.

Most of these field and laboratory studies have concentrated on measurements of electrical fields as they require simple and cheap instrumentation. The investigation of seismo-magnetic fields has received much less attention, mainly because of the complex apparatus for measuring low magnetic fluxes. As suggested by Pride & Haartsen (1996), the seismo-electric field E has to be associated to the whole seismic field whereas the seismo-magnetic field B is coupled to transverse modes (S waves). To our knowledge, no study succeeded to confirm the theoretically predicted seismo-magnetic field: neither its existence nor its magnitude. In a recent short paper Bordes et al. (2006) announced that seismo-magnetic couplings were measurable at least in low magnetic noise environment and consistent with these theoretical predictions. In this paper, the seismic, seismo-electric and seismo-magnetic field were compared, but these preliminary results were not fully interpreted and seismo-magnetic amplitudes were not given.

To go further, this paper describes with details the original experimental apparatus and presents arguments to give seismo-magnetic amplitudes. This experiment was built in the ultra-shielded chamber of the Low Noise Underground Laboratory of Rustrel (France) to measure seismo-electromagnetics of the co-seismic type. It is shown that very weak residual vibrations can generate strong disturbing co-seismic signals that could be misinterpreted. We point out that devices for seismo-magnetic couplings measurements have to be very carefully designed for experimental measurements as well as for field investigations.

The major difficulty blocking access to seismomagnetic amplitudes is due to magnetometers, which are sensitive both to radial and azimuthal components of

the magnetic field. As this dependence differs strongly according to the component (10 V/nT for radial and 10 mV/nT for azimuthal component), the access to real amplitudes can be a difficult task. However, analytical developments adapted to our experiment configuration showed that the radial component is negligible. It allowed to provide an estimation of the measured seismomagnetic field amplitude around 0.035 nT for a 1 $m.s^{-2}$ seismic source.

2 Seismic to electromagnetic field conversion: theoretical background

The equations governing the coupled seismic and electromagnetic wave propagation in a fluid-saturated porous medium have been developed by Pride (1994). In his work, this author derived a complete set of nine macroscopic equations, grouping into four Maxwell's and three poroelastic equations which are connected by two transport relations [(Pride, 1994) equations (250) and (251)]:

$$\mathbf{J} = \sigma(\omega)\mathbf{E} + L(\omega)\left(-\nabla p + \omega^2 \rho_f \mathbf{u_s}\right) \tag{1}$$

$$-i\omega\mathbf{w} = L(\omega)\mathbf{E} + \frac{k(\omega)}{\eta}\left(-\nabla p + \omega^2 \rho_f \mathbf{u_s}\right) \tag{2}$$

In equation 1, the macroscopic electrical current density $\mathbf{J}$ is written as the sum of the average conduction and streaming current densities. Similarly, the fluid flux $\mathbf{w}$ of equation 2 is separated into electrically and mechanically induced contributions. The electrical fields and mechanical forces that generate the current density $\mathbf{J}$ and fluid flux $\mathbf{w}$ are, respectively, $\mathbf{E}$ and $(-\nabla p + i\omega^2 \rho_f \mathbf{u_s})$, where p is the pore-fluid pressure, u_s is the solid displacement, and $\mathbf{E}$ is the electric field. In the above relationships, ρ_f is the pore-fluid density, η is the fluid's shear viscosity, and ω is the angular frequency. The most important parameter in equations 1 and 2 is the complex and frequency-dependent electrokinetic coupling coefficient $L(\omega)$, which describes the coupling between the seismic and electromagnetic fields (Pride, 1994; Reppert et al., 2001):

$$L(\omega) = L_0 \left[1 - i \frac{\omega}{\omega_c} \frac{m}{4} \left(1 - 2 \frac{d}{\Lambda} \right)^2 \left(1 - i^{3/2} d \sqrt{\frac{\omega \rho_f}{\eta}} \right)^2 \right]^{-\frac{1}{2}} \tag{3}$$

where the static electrokinetic coupling is given by:

$$L_0 = -\frac{\phi}{\alpha_\infty} \frac{\varepsilon_{rf}\, \zeta}{\eta} \left(1 - 2 \frac{d}{\Lambda} \right) \tag{4}$$

where m and Λ are geometrical parameters of the pores given in table C, ϕ is the porosity, α_∞ the tortuosity, d the Debye length and ε_{rf} the dielectric constant of the fluid. The critical angular frequency ω_c defined in the Biot's theory separates the viscous and inertial flow domains. Its value depends on the permeability k_0:

$$\omega_c = \frac{\phi}{\alpha_\infty k_0} \frac{\eta}{\rho_f} \tag{5}$$

The remaining two coefficients $\sigma(\omega)$ and $k(\omega)$ of equations 1 and 2, represent the electric conductivity and dynamic permeability of the porous material, respectively. These coefficients are detailed in appendix A.1. The most influencing parameter on the electrokinetic coupling coefficient (equations 3 and 4) is the electrical potential at the rock/fluid interface (called zeta potential), itself depending on fluid composition, pH, and formation factor (Davis et al., 1978; Ishido & Mizutani, 1981; Jouniaux & Pozzi, 1995a; Lorne et al., 1999a; Jouniaux et al., 2000; Guichet et al., 2006).

In light of Pride's theory, Garambois & Dietrich (2001) expressed the electric and magnetic fields $\mathbf{E}$ and $\mathbf{H}$ as a function of the seismic displacement $\mathbf{u}$. In case of plane waves propagating in the homogeneous medium at seismic frequencies ($\omega < \omega_c$), they found:

$$\mathbf{E} \simeq \frac{1}{\sigma_f} \frac{\varepsilon_0\, \rho_f\, \kappa_f\, \zeta}{\eta} \left(1 - \frac{\rho}{\rho_f} \frac{C}{H} \right) \ddot{\mathbf{u}} \tag{6}$$

for displacements associated to the longitudinal fast (type I) P-waves (Biot, 1956, 1962), and

$$|\, \mathbf{H} \,| \simeq \frac{\phi}{\alpha_\infty} \frac{\varepsilon_0\, \rho_f\, \kappa_f\, |\zeta|}{\eta} \sqrt{\frac{G}{\rho}}\, |\dot{\mathbf{u}}| \tag{7}$$

for displacements associated to transverse SH- and SV-waves.

Note that the seismo-magnetic field is coupled to the transverse propagation mode. The in-line component E of the electric field accompanying the compressional waves is therefore approximately proportional to the grain acceleration. In expressions 6 and 7, ε_0 is the vacuum's dielectric constant and σ_f represents the fluid's electric conductivity, G is the shear modulus of the framework, ϕ is the porosity, and ρ is the bulk density. The tortuosity α_∞ represents a geometrical factor depending on the pore structure and orientation, and is usually taken equal to the product of the porosity by the formation factor. The definitions of the C and H moduli are those of Biot (1962) (appendix A.1).

However, boundary conditions can produce significant effects on the seismic propagation and have to be taken into account for the seismo-electromagnetic interpretations. In the experiment described afterwards, the sand is placed in a cylindrical column. Therefore extensional modes have to be taken into account. As an illustration, analytical solutions of the seismo-electromagnetic fields are developped in appendix B. Moreover, we will show in section 5 that the vertical seismic excitation should induce an azimuthal magnetic field in such a configuration.

3 Experimental setup

3.1 Underground low magnetic noise laboratory

Since the decommissioning of the ground-based component of the French nuclear missile system, the underground control chamber has been turned into an underground low magnetic noise laboratory. The LSBB (Laboratoire Souterrain à Bas Bruit, Rustrel France) presents very low electromagnetic noise conditions which give the possibility to perform very sensitive electromagnetic measurements. At the deepest point (500 m below the surface), a non-conventional shielded cylindrical capsule is embedded without any μ-metal. The chamber is suspended on massive springs cutting off low frequency ground motions with a residual electromagnetic noise lower than 2 $fT/\sqrt{Hz}$ above 10 Hz (Waysand et al., 1999; Gaffet et al., 2003). To preserve these outstanding conditions, sen-

sitive parts of the experiment including sample, seismic source and sensors, are located within the ultra-shielded chamber. On the contrary, the instruments generating electromagnetic disturbances (electronic devices) are placed outside the chamber, within the corridor (figure 1).

[Figure 1 about here.]

3.2 Characteristics of the porous medium

Physico-chemical properties of the mineral grains are of the highest importance on seismo-electromagnetic couplings. Especially, the grains have to be poorly soluble to avoid increasing of the fluid conductivity and decreasing of the electrokinetic coupling (see equation 6). Consequently, we chose a highly referenced medium for mechanical, electrical and chemical properties composed with 99 % of silica. A Plexyglas column 104 cm long and 8 cm diameter (figure 2, part A) is filled with Fontainebleau sand that can be imbibed from below with demineralized water to obtain high electrokinetic couplings (Guichet et al., 2003; Lorne et al., 1999a). The sand was highly compacted by about 1500 hammer shots during the filling in order to limit the high frequency attenuation. The measured permeability of the sand is 5.8 10^{-12} m^2, its electrical resistivity is 22 $k\Omega.m$, and the water conductivity is 3.1 $mS.m^{-1}$ with a pH of 6.55 at 20.5 $°C$.

The bulk density of the sand (1.77 10^3 $kg.m^{-3}$) has been measured by weighing during the filling. By comparing to the bulk density of silica (2.65 10^3 $kg.m^{-3}$), we obtain the total porosity of the sand (33%) which is constant along the sample. On the other hand, the volume of water imbibed in the sand does not exceed 1.9 L. The sand has been fluid filled by imbibition from a water tank connected to the lower extremity. This procedure does not allow to acquire a fully saturated sample, but rather in the range of 80 to 95%.

3.3 Experimental setup within the ultra-shielded chamber

Seismic wave propagation is generated by a pneumatic seismic source (Bordes et al., 2006) able to reproduce a large number of identical impacts within a few

minutes. This system was carefully designed to be free of electromagnetic noise and to allow stacking in order to improve the signal to noise ratio. The impact is obtained by launching a ruby ball on a granite plate. The time source function is recorded by an accelerometer fixed on the plate and exhibits a broad band spectra from 150 Hz to 10 kHz (Bordes et al., 2006). Seismic excitation is vertically polarized and the seismic propagation contains longitudinal (compressive), transverse (shear) and extensional modes.

[Figure 2 about here.]

Seismo-magnetic couplings associated to the seismic propagation can be measured with two induction magnetometers. The first one, in the upper position, can be placed in 7 different locations whereas the second one is fixed as a reference position (figure 2, part A). Each magnetometer is divided into two elements (figure 2, part B) which can be splitted to be placed around the column without any contact with the sample. Each element consists in a magnetic core focussing magnetic fluxes. These fluxes generate induction currents in the coils that are finally amplified and recorded.

These magnetometers are sensitive both to radial and azimuthal components of the magnetic field and the output consists in one channel. As a consequence, getting real amplitudes needs to expect or at least to assume a field polarization. Sensitivities are given in figure 2, part C, where grey and black lines represent respectively lower and upper magnetometer. The radial sensitivity was calibrated by measuring magnetic fluxes generated by a calibration coil placed in the symetry axis of the magnetometers. It is almost constant, nearly 10 V/nT, in the 100 to 1000 Hz range. The azimuthal sensitivity was calibrated by measuring fluxes generated by a vertical wire in the magnetometer's symetry axis and is rounded to 10 mV/nT in order to give an order of magnitude of azimuthal fields.

[Figure 3 about here.]

3.4 Remote control of the experimental setup

To avoid strong electromagnetic disturbances from electronic devices, the whole experiment was remote controlled from the corridor of the laboratory (figure 3). It includes the seismic source driving, the charge amplifier of the accelerometer, and the acquisition system. All measurements were performed using a 24 bit seismic recorder (Geometrics StrataVisor NZ) using a 21 μs time sampling rate. The source driving system consists in an electrovalve supplied by a pulse generator (24 V/256 ms) whose input is protected from a possible discharge of the coil by a freewheel diode. This driving system is enclosed in a ground connected shielding box to avoid the transmission of electromagnetic disturbances from the electrovalve to the acquisition wires.

4 Seismo-magnetic measurements

4.1 Necessity of exceptional care for seismo-magnetic measurements

Seismo-magnetic measurements need carefully designed experimental apparatus to avoid electromagnetic disturbances. Especially, it is essential to avoid those due to the seismic triggering. All disturbances occuring using the seismic source trigger would be stacked and could distort or mask real signals. Indeed as the permanent magnetic field is 10 times smaller than in usual conditions, the moving of conductive or magnetic material can generate some strong disturbances from induction origin. Thus, the stainless steel ball and the metallic spring we choose at the beginning of the experiment was replaced by a ruby ball and a rubber band in the final free noise seismic source. Moreover, all metallic screws of the experimental apparatus were replaced by nylon screws. Only the copper tube of the seismic source, poorly moving and non-magnetic, was preserved to be ground-connected and avoid an electrostatic charge accumulation.

Once this simple care taken, most serious disturbances occur when the magnetometer standing have mechanical contacts with the sample. Indeed, if vibrations due to the seismic propagation are transmitted to the magnetometers, a transient magnetic field is measured but is not related to any electrokinetic

origin. These signals, due to the transient moving of the magnetometer in the permanent magnetic field, can not be distinguished from electrokinetically generated seismo-magnetic field.

The experimental apparatus was anticipated to avoid these disturbances: the magnetometers and the sample were fixed on two differents stands (figure 2, part A). Thereby, there is no contact between the sample and the magnetometers (figure 2, part B). However, residual seismic waves can be transmitted to the floor and then to the magnetometer stand. To illustrate this phenomena, we recorded the horizontal and vertical residual vibrations of the upper magnetometer occuring after one shot (figure 4). This simple test clearly shows that the magnetometer's vibrations are very weak and measurable by accelerometers ($< 2.10^{-3}$ m.s^{-2} on the horizontal but negligible on the vertical accelerometer, part A). In this case, corresponding magnetic signals show a strong 80 Hz/8 mV signal probably corresponding to the resonant frequency of the magnetometers stands. This phenomena can be strongly attenuated by introducing a sound-proofing protection on the floor (figure 4 part B) but cannot be totally cancelled (in the range of 2 mV). In the next section, it will be shown that these disturbances are delayed with respect to the seismic propagation in the sample and are out of the time window of interest (0-2 ms).

[Figure 4 about here.]

4.2 Results

The existence of the theoretically predicted seismo-magnetic conversions can be studied by comparing seismic and magnetic signals in dry and moist sand. Such a comparison allows to separate as an evidence coherent magnetic signals identified as disturbances from those generated by electrokinetic effects. Indeed, the electrokinetic effects occur only when water is present (Guichet et al., 2003), as shown in the figure 5. Seismo-magnetic sections presented were obtained by stacking 100 records of the upper magnetometer at the seven possible locations. Corresponding seismic records obtained on an identical apparatus are given to show the comparison of seismic and seismo-magnetic propagations. The grey

zone is jointly defined for seismic and magnetic sections only to highlight the location of first arrivals.

All sections are trace by trace normalized to emphasize the propagation phenomena. This figure clearly shows that coherent magnetic arrivals appear when the sand is fluid-filled. This comparison of measurements in dry and moist sand gives arguments to show the electrokinetic origin of the transient magnetic field. These seismo-magnetic signals are the first kind of the seismo-magnetic conversion, and are travelling with the seismic wave within the moist sand.

[Figure 5 about here.]

4.2.1 Comments on amplitudes

In order to find a representative event in the seismic and magnetic sections, we picked the negative polarity of first arrival as it is the cleanest in the seismo-magnetic records. The maximum negative amplitudes were measured within the grey area and plotted on the right of each section. Furthermore, the occurrence of seismomagnetic phenomena in fluid-filling sand is highlighted by the comparison of the first arrival amplitude (black line) with the average noise level recorded before the impact (grey line). In order to respect a meticulous interpretation of the data, the maximum amplitude values correspond to the output of the magnetometer (mV). Indeed, the discussion on real magnetic amplitudes needs a complete analytical discussion given in section 5

As evoked above, Garambois & Dietrich (2001) showed that seismo-magnetic signals are proportional to the S-waves grain velocity in the low frequency approximation. Using the same procedure, we show in appendix B that the azimuthal seismo-magnetic field should be proportional to the radial grain velocity associated to transverse waves. In the moist sand the amplitude of the seismo-magnetic signal decreases from the top to the bottom of the column, mainly because the seismic energy decreases from the impact seismic source. Full waveform of seismic and seismo-magnetic signals are similar, however, a complete comparison of magnetic and seismic fields would be not appropriate in this case. Indeed, the seismic source generates P, S and extensional waves, but the different seismic modes can not be separated because of the too small sam-

ple length and because accelerometers measure the axial component of the grain acceleration. Thus, it is impossible to choose an event in the seismic signals that could be directly associated to S waves and compared to the seismo-magnetic field.

The comparison of the magnetic amplitudes in dry and moist sand shows as an evidence that the seismo-magnetic conversions are very weak. A comparison of maximum amplitudes of the grey zones in magnetic signals show that signals in moist sand (0.3 mV at 10 cm) are only 6 times larger than in dry sand (0.05 mV at 10 cm). It is interesting to note that the signal to noise ratio is better in moist sand, partly due to a lower noise level in moist sand. Indeed, real noise amplitudes measured before the triggering are significantly lower in moist (0.02 mV) than in dry sand (0.05 mV).

The conversion to real magnetic amplitude values needs the assumption of a purely azimuthal or radial field. According to the major polarization of the magnetic field, this amplitude could vary from 0.035 pT to 0.035 nT for a $1\,m.s^{-2}$ seismic source. This topic will be discussed in the light of the analytical approach of seismo-electromagnetic fields of the section 5.

4.2.2 Comments on propagation velocities

One of the most significant results is obtained by comparing seismic and seismo-magnetic propagation velocities by picking first breaks on enlarged views of the seismic and magnetic sections (figure 6). A careful analysis in the $[0 - 1.5\ ms]$ window of the magnetic records on dry and moist sand shows a residual disturbance arising at $t = 0\,s$. This phenomenon exhibits amplitude of the same order as the signal. Then, it is invisible on the one shot record but appears after the stacking procedure. It is due to the seismic triggering and can be due to crosstalk (from time source function recording) or to electromagnetic disturbances by the impact. This disturbance has to be eliminated, or at least attenuated, to enable the computing of the apparent velocity of the seismo-magnetic wave within the compacted sand.In order to minimize this phenomenon, the lower magnetometer was used as a reference. The subtraction of the reference from each point of measurement improves the data by minimizing the distur-

bance and unmasking the first breaks of interest (figure 6).

This subtraction enables us to deduce the apparent velocity of the seismo-magnetic field ($791 \pm 80\, m.s^{-1}$) with a better signal to noise ratio. This velocity can be compared to the significantly faster seismic velocities. The measured seismic velocities are almost the same in dry ($1201 \pm 85\, m.s^{-1}$) and moist sand ($1328 \pm 94\, m.s^{-1}$). These values are consistent with P-waves velocities measured by Elliott & Wiley (1975) in partially saturated compacted sample (Ottawa sand, porosity 30 %).

The fact that any significative increase in seismic velocity with fluid filling is not observed is consistent with laboratory measurements of Knight & Nolen-Hoeksema (1990). They showed that the behavior of the P-wave velocity with increasing water-saturation within sandstones strongly depends on the means used to saturate the porous medium. In the imbibition case, the P-wave velocity is increased only after 80% of water-saturation (and is constant below), whereas in drainage conditions the P-wave velocity is increased with water-content as soon as 45% of water saturation (see also Gist 1994). Since the seismic velocities in our dry and moist sand are the same (given the associated errors), and because we are in imbibition conditions, we can deduce that the sand is partly saturated, probably with a maximum of 80%-85% of water saturation.

[Figure 6 about here.]

In the present section we proved that seismo-magnetic phenomena in partly saturated sand have an electrokinetic origin. The velocity of the seismo-magnetic field is measured to be lower than the seismic velocity. In order to improve interpretations of velocities and to better understand seismomagnetic amplitudes, an analytical approach of the seismo-electromagnetic couplings including the geometrical characteristics of our experimental setup is proposed. Indeed, under a vertical seismic excitation in a cylindrical porous medium, specific modes can be generated due to the presence of the free cylindrical surface. In the next section we calculate the extensional phase velocity and deduce that the fast seismic arrivals are associated to the P and extensional waves, and that the slower seismo-magnetic arrivals are associated to S-wave.

5 Analytical approach for seismo-electromagnetic fields interpretations

The description of the complete seismic propagation needs to take into account the fast (P_f) and slow (P_s) longitudinal modes, the transverse modes (S) as well as the specific modes due to the cylindrical free surface. Considering the axial seismic excitation, we assume that these specific modes are only extension and we neglect flexion and torsion (Dunn, 1986). The goal of this analytical approach is to evaluate expected phase velocities of the different waves, in order to identify which waves are converted into seismo-electromagnetic fields. We show that V_{ext} and V_{P_f} are very close unless the sand is not totally fluid-filled. Moreover, we show that in a cylindrical porous medium under a vertical excitation, the induced seismo-magnetic field should be azimuthal.

5.1 Seismic velocities of body waves

In order to compute the phase velocity of the extensional mode, the bulk (K_{fr}) and shear (G) frame moduli of the sand have to be estimated. Then, K_{fr} can be deduced from inversion of the measured P_f wave velocity. Indeed, suitable moduli can be calculated from observations using expressions of phase velocities:

$$V_{Pf} = \frac{1}{Re(s_{Pf})} \qquad V_{Ps} = \frac{1}{Re(s_{Ps})} \qquad V_S = \frac{1}{Re(s_S)} \tag{8}$$

where s_{Pf}, s_{Ps} and s_S are slownesses of P_f, P_s and S waves from Pride & Haartsen (1996) (equations 30, 31 and 33 of appendix A.2).

As it was evoked above, our fluid-filling method (imbibition) does not enable us to obtain a fully saturated sample and the seismic velocities in dry and moist sand are very close. Indeed, Knight & Nolen-Hoeksema (1990) showed that during the imbibition procedure, the P_f wave velocity is quite constant until the saturation coefficient exceeds 85%. A computation of phase velocities needs to take into account the partial saturation. Since the velocity change is negligible in the 0 to 80% saturation range, a first order approximation of the frame modulus can be obtained by considering that the fluid is totally replaced by air. In this case, the computation of the P_f-wave velocity from expressions 8

versus frame modulus shows that the measured 1250 $m.s^{-1}$ velocity corresponds to a unique value of the frame modulus $K_{fr} = 1.2\ 10^9\ Pa$ (figure 7). This value is larger than the usually assumed values for sand, which are around $[0.1 - 0.5\ GPa]$ (Garambois & Dietrich, 2001; Karner et al., 2003; Block & Harris, 2003, 2006). However this value is within the range $[0 - 4.2\ GPa]$ proposed by Hickey & Sabatier (1997) for modeling water-saturated sand.

[Table 1 about here.]

On the other hand, the shear modulus $G \simeq 1.32\ 10^9\ Pa$ can be inferred considering the ratio $K_{fr}/G = 0.9$ from Murphy et al. (1993) for quartzic granular media. This computation shows that the S-wave velocity can be estimated to 860 $m.s^{-1}$ from these deduced moduli in the dry sand (figure 7). Assuming that this first order inversion in dry sand can not introduce strong errors, the calculated frame bulk and shear moduli values will be used in the next section to compute the phase velocity of the extensional mode.

[Figure 7 about here.]

5.2 Extensional modes

Considering the vertical seismic source, some specific modes can be generated on the free cylindrical surface of the sample from interferences of P and S waves. Extensional modes occuring in water saturated porous media have been early studied by Gardner (1962) for quantitative interpretation of seismic velocities in resonant bars. Using this approach, numerical computation of Dunn (1986) show specific dispersion and attenuation effects in cylindrical samples of sandstones. In this case, the phase velocity of extensional modes is smaller than P_f but larger than S wave phase velocity. A first order approximation of the extensional phase velocity can be obtained from the *bar velocity* given by:

$$V_{ext} = \sqrt{\frac{E}{\rho}} \tag{9}$$

where E is the Young's modulus usually defined in elastic media, and can be measured for rock samples as the slope of an axial stress versus axial strain

curve from a deformation test. We can use this expression for the porous media by substituting the elastic moduli K by the equivalent Gassman moduli K_G:

$$E = \frac{9\ K_G\ G}{3K_G + G} \tag{10}$$

where K_G, the Gassman's modulus defined in appendix C and A.1, represents the equivalent K modulus for the porous media. A prediction of the phase velocities in the partially saturated sand can be obtained by using an average on the density ρ_f and the bulk modulus K_f versus the saturation coefficient S_w:

$$\rho_f(S_w) = S_w\ \rho_{water} + (1 - S_w)\ \rho_{air} \tag{11}$$

and

$$K_f(S_w) = \left[\frac{S_w}{K_{water}} + \frac{1 - S_w}{K_{air}}\right]^{-1} \tag{12}$$

In the following expressions, we will take into account the partial saturation by substituting K_f and ρ_f by their average values. Finally, an estimation of the extension's phase velocity in the partially saturated sample can be computed from:

$$V_{ext}(S_w) = \sqrt{\frac{9\ K_G(S_w)\ G}{\rho(S_w)\ [\ 3K_G(S_w) + G\ ]}} \tag{13}$$

A computation of equations 11, 12, 13, and 8 respectivly predicts 1250 $m.s^{-1}$ and 1260 $m.s^{-1}$ phase velocities for extensional and P waves in dry sand (figure 8). These velocities respectively increase to 1315 $m.s^{-1}$ and 2050 $m.s^{-1}$ for the water-saturated sand. This result is consistent with the work of Dunn (1986) showing a $V_{ext}/V_S = 1.6$ ratio. The P-wave velocity is strongly increased by water only when approaching the water-saturation state. Since the extensional waves are induced by interferences of S and P waves, the extensional wave is also fastened. Finally, this computation clearly shows that the P_f and extension modes are very difficult to distinguish in partial saturation conditions, at least by considering the first break of seismic arrival. Thus, the seismic arrivals recorded in the sample showing a 1200/1300 $m.s^{-1}$ velocity will be associated

to P and extensional waves. Slow events with 800/900 $m.s^{-1}$ velocities will be associated to S-waves.

[Figure 8 about here.]

5.3 Seismo-magnetic field polarization

As a complement of the seismic velocities analysis, a complete formulation of seismo-electromagnetic fields is required to propose a correct interpretation of the measurements, especially for the seismo-magnetic field polarization and magnitude. Seismo-electromagnetic fields can be expressed from seismic displacements via appropriate coefficients for each propagation mode (Pride & Haartsen, 1996). As reminded in appendix B, displacements associated to P_f and P_s waves are described by the scalar potentials ϕ_f and ϕ_s whereas S waves displacements can be represented by the vector potential Γ_S.

The seismo-magnetic field is derived from the Maxwell equation:

$$\mathbf{H} = -\frac{i}{\omega\,\mu}\,(\nabla \times \mathbf{E}) \tag{14}$$

where μ is the magnetic permeability of the free space, and H and E are respectively the seismo-magnetic and seismo-electric fields. Indeed, the purely longitudinal part of the seismic propagation (P waves) does not contribute to the seismo-magnetic field and only S and extensional waves can produce co-seismic magnetic effects. In appendix B, we showed that the seismo-magnetic field generated from S waves (H_S) and from extensional waves (H_{ext}) are expressed by:

$$H_{s,\theta} = -\frac{\phi}{\alpha_\infty}\frac{\epsilon_0\,\kappa_f\,\zeta}{\eta}\rho_f\,\sqrt{\frac{G}{\rho}}\,\frac{du_{s,r}}{dt} \tag{15}$$

and

$$H_{e,\theta} = -\frac{\phi}{\alpha_\infty}\frac{\epsilon_0\,\kappa_f\,\zeta}{\eta}\rho_f\,\sqrt{\frac{E}{\rho}}\,\frac{du_{s,r}}{dt} \tag{16}$$

Whatever the origin of the seismo-magnetic field is, the only non-zero component is the azimuthal one and the analytical prediction shows that the measured magnetic field should be azimuthal. Even if it is not possible to rule very

weak radial perturbations, it is reasonable to assume that they are negligible. These results are consistent with the study of Hu & Wang (2000) for a fluid-filled borehole and give fundamental arguments for the interpretation of the seismo-magnetic measurements. Indeed, it is possible to assume that the quantification of amplitudes needs to take into account the azimuthal sensitivity of the magnetometers.

6 Discussion and conclusion

The exceptional environment and facilities of the Low Noise Underground Laboratory of Rustrel gave us the possibility to build a carefully designed experimental setup for seismo-magnetic measurements in moist sand. The seismic arrivals recorded in the sample shows a $1328 \pm 94\ m.s^{-1}$ velocity and have been associated to P and extensional waves in the partially saturated sand. We calculated a S-wave velocity of 800 to 900 $m.s^{-1}$. The measured seismo-magnetic arrivals shows a velocity of about $791 \pm 80\ m.s^{-1}$. Therefore, we propose that the seimo-magnetic field is electrokinetically induced and is associated to S-wave propagation. This was theoretically predicted by Pride (1994), but never measured up to now.

Magnetic measurements were performed with two induction magnetometers whose radial and azimuthal resolution are respectively around 10 V/nT and 10 mV/nT for a maximal amplitude of $0,35\ mV$ in output of the magnetometers. Applying the Pride's theory for seismo-electromagnetic couplings, we show that the seismo-magnetic field is purely azimuthal. Even if it is very difficult to rule out the possibility of very weak non-axial vibrations, generating radial magnetic field, it is reasonable to conclude that the measured amplitudes are in the order of 0.035 nT for a 1 $m.s^{-2}$ seismic source. Further studies, implying the measurement of the three components of the magnetic field, are necessary to definitely conclude on the seismo-magnetic amplitudes. In order to better understand the seismo-magnetic conversions, further numerical, field and laboratory investigations are needed. To this end, the LSBB facilities give exceptional possibility to measure seismo-electromagnetic couplings in porous

media.

Usual field seismic sources are explosives, vibroseis or sledgehammer blows which induce accelerations values in the range of 0.05 to 100 $m.s^{-2}$ (table 2). In the assumption of amplitudes about 0.03 nT for a 1 $m.s^{-2}$ seismic source, field seismo-magnetic measurements could be performed out of the low noise environment. Nevertheless, extra care has to be taken to ensure the electrokinetic origin of the measurements. Especially, magnetometers have to be isolated from ground motions as well as from coherent electromagnetic noise. Thus, borehole measurements would be very difficult, because of unavoidable contacts between the tool and the mud transmitting ground vibrations. Nevertheless, subsurface measurements could be performed with ingenious experimental apparatus including a strong stacking procedure to improve the signal to noise ratio.

[Table 2 about here.]

7 Acknowledgements

This work was supported by the French National Scientific Research Center (CNRS), and "ACI Eau et Environnement" of the French Ministry of Research. We are grateful to G. Waysand for helpul discussions and authorization to perform this experiment in the LSBB laboratory. We thank M. Auguste, D. Boyer, A. Cavaillou, G. Clerc, R. Guiguet, and Y. Orengo for their technical help.

References

Ageeva, O. A., Svetov, B. S., Sherman, G. K., & Shipulin, V., 1999. E-effect in rocks., *Russian Geology and Geophysics*, **64**, 1349–1356.

Beamish, D., 1999. Characteristics of near surface electrokinetic coupling, *Geophys. J. Int.*, **137**, 231–242.

Biot, M. A., 1956. Theory of propagation of elastic waves in a fluid-saturated porous solid: I. low frequency range, *J. Acoust. Soc. Am.*, **28**(2), 168–178.

Biot, M. A., 1962. Mechanics of deformation and acoustic propagation in porous media, *J. Appl. Phys.*, **34**(1), 36–40.

Block, G. & Harris, J. G., 2003. Coupled electrokinetic-biot theory and measurement techniques in sediment acoustics, *16th ASCE Engineering Mechanics Conference, University of Washington, Seattle*.

Block, G. I. & Harris, J. G., 2006. Conductivity dependence of seismoelectric wave phenomena in fluid-saturated sediments, *J. Geophys. Res.*, **111**, B01304.

Bordes, C., Jouniaux, L., Dietrich, M., Pozzi, J.-P., & Garambois, S., 2006. First laboratory measurements of seismo-magnetic conversions in fluid-filled fontainebleau sand, *Geophys. Res. Lett.*, **33**, LO1302.

Broding, R. A., Buchanan, D., & P.Hearn, D., 1963. Field experiments on the electroseismic effect, *IEEE Transactions on geoscience electronics*, **GE-1**, 23–31.

Butler, K. E. & Russell, R. D., 1993. Substraction of powerline harmonics from geophysical records, *Geophysics*, **58**, 898–903.

Chandler, R., 1981. Transient streaming potential measurements on fluid-saturated porous structures: An experimental verification of biot's slow wave in the quasi-static limit, *J. Acoust. Soc. Am.*, **70**, 116–121.

Chen, B. & Mu, Y., 2005. Experimental studies of seismoelectric effects in fluid-saturated porous media, *Journal of Geophysics and Engineering*, **2**, 222–230.

Cooke, C. E., 1955. Study of electrokinetic effects using sinusoidal pressure and voltage, *J. Chem. Phys.*, (23), 2299–2303.

Davis, J. A., James, R. O., & Leckie, J., 1978. Surface ionization and complexation at the oxide/water interface, *Journal of Colloid and Interface Science*, **63**, 480–499.

Doussan, C., Jouniaux, L., & Thony, J.-L., 2002. Variations of self-potential and unsaturated flow with time in sandy loam and clay loam soils, *Journal of Hydrology*, **267**, 173–185.

Dunn, K.-J., 1986. Acoustic attenuation in fluid-saturated porous cylinders at low frequencies, *J. Acoust. Soc. Am.*, **79**(6), 1709.

Dupuis, J. C. & Butler, K. E., 2006. Vertical seismoelectric profiling in a borehole penetrating glaciofluvial sediments, *Geophys. Res. Lett.*, **33**.

Dupuis, J. C., Butler, K. E., & Kepic, A. W., 2007. Seismoelectric imaging of the vadose zone of a sand aquifer, *Geophysics*, **72**, A81–A85.

Elliott, S. E. & Wiley, B. F., 1975. Compressional velocities of partially saturated, unconsolidated sands, *Geophysics*, **40**(6), 949–954.

Gaffet, S., Guglielmi, Y., Virieux, J., Waysand, G., Chwala, A., Stolz, R., Emblanch, C., Auguste, M., Boyer, D., & Cavaillou, A., 2003. Simultaneous seismic and magnetic measurements in the low-noise underground laboratory (lsbb) of rustrel, france, during the 2001 january 26 indian earthquake, *Geophys. J. Int.*, **155**, 981–990.

Garambois, S. & Dietrich, M., 2001. Seismoelectric wave conversions in porous media: Field measurements and transfer function analysis., *Geophysics*, **66**, 1417–1430.

Garambois, S. & Dietrich, M., 2002. Full waveform numerical simulations of seismoelectromagnetic wave conversions in fluid-saturated stratified porous media., *J. Geophys. Res.*, **107**(B7).

Garambois, S., Senechal, P., & Perroud, H., 2002. On the use of combined geophysical methods to access water content and water conductivity of near surface formations., *Journal of Hydroloy*, (259), 32–48.

Gardner, G. H. F., 1962. Extensional waves in fluid-saturated porous cylinders, *J. Acoust. Soc. Am.*, **34**(1), 36–40.

Gaskarov, I. & Parkhomenko, E., 1974. The seismoelectric effect in rocks and the preconditions for its application in geological prospecting work, *Izv. Akad. Sci. USSR, Physics Solid Earth*, **1**, 71–74.

Gist, G. A., 1994. Interpreting laboratory velocity measurements in partially gas-saturated rocks, *Geophysics*, **59**(7), 1100–1109.

Guichet, X., Jouniaux, L., & Pozzi, J.-P., 2003. Streaming potential of a sand column in partial saturation conditions, *J. Geophys. Res.*, **108**(B3).

Guichet, X., Jouniaux, L., & Catel, N., 2006. Modification of streaming potential by precipitation of calcite in a sandwater system: laboratory measurements in the ph range from 4 to 12, *Geophys. J. Int.*, **166**.

Haartsen, M. W. & Pride, S., 1997. Electroseismic waves from point sources in layered media., *J. Geophys. Res.*, **102**, 24,745–24,769.

Haartsen, M. W., Dong, W., & Toksöz, M. N., 1998. Dynamic streaming currents from seismic point sources in homogeneous poroelastic media, *Geophys. J. Int.*, **132**, 256–274.

Haines, S. S., Guitton, A., & Biondi, B., 2007. Seismoelectric data processing for surface surveys of shallow targets, *Geophysics*, **72**, G1–G8.

Haines, S. S., Pride, S. R., Klemperer, S. L., & Biondi, B., 2007. Seismoelectric imaging of shallow targets, *Geophysics*, **72**, G9–G20.

Hart, D. J. & Wang, H. F., 1995. Laboratory measurements of a complete set of poroelastic moduli of berea sandstone and indiana limestone, *J. Geophys. Res.*, **100**(B9), 17.741–17.751.

Hase, H., Ishido, T., Takakura, S., Hashimoto, T., Sato, K., & Tanaka, Y., 2003. Zeta potential measurement of volcanic rocks from aso caldera, *Geophys. Res. Lett.*, **23**(30), 2210.

Hickey, C. J. & Sabatier, J. M., 1997. Choosing biot parameters for modeling water-saturated sand, *J. Acoust. Soc. Am.*, **102**, 1480–1484.

Hu, H. & Wang, K., 2000. Simulation of an acoustically induced electromagnetic field in a borehole embedded in a porous formation, *Borehole Acoustics and Logging Reservoir Delineation consortis, Annual Report*, pp. 13–1 – 13–20.

Hunt, C. W. & Worthington, M. H., 2000. Borehole elektrokinetic responses in fracture dominated hydraulically conductive zones, *Geophys. Res. Lett.*, **27**(9), 1315–1318.

Ishido, T. & Mizutani, H., 1981. Experimental and theoretical basis of electrokinetic phenomena in rock water systems and its applications to geophysics, *J. Geophys. Res.*, **86**, 1763–1775.

Jackson, M. D., Saunders, J. H., & Addiego-Guevara, E. A., 2005. Development and application of new downhole technology to detect water encroachment toward intelligent wells, *Society of Petroleum Engineers, annual technical conference*.

Jiang, Y. G., Shan, F. K., Jin, H. M., & Zhou, L. W., 1998. A method for measuring electrokinetic coefficients of porous media and its potential application in hydrocarbon exploration, *Geophys. Res. Lett.*, **25**(10), 1581–1584.

Johnson, D. L., Koplik, J., & Dashen, R., 1987. Theory of dynamic permeability in fluid saturated porous media, *J. Fluid. Mech.*, **176**, 379–402.

Jouniaux, L. & Pozzi, J.-P., 1995. Permeability dependance of streaming potential in rocks for various fluid conductivity, *Geophys. Res. Lett.*, **22**, 485–488.

Jouniaux, L. & Pozzi, J.-P., 1995. Streaming potential and permeability of saturated sandstones under triaxial stress: consequences for electrotelluric anomalies prior to earthquakes, *J. Geophys. Res.*, **100**, 10,197–10,209.

Jouniaux, L. & Pozzi, J.-P., 1997. Laboratory measurements anomalous 0.1-0.5 hz streaming potential under geochemical changes: Implications for electrotelluric precursors to earthquakes, *J. Geophys. Res.*, **102**, 15,335–15,343.

Jouniaux, L., Bernard, M.-L., Zamora, M., & Pozzi, J.-P., 2000. Streaming potential in volcanic rocks from mount peleé, *J. Geophys. Res.*, **105**, 8391–8401.

Karner, S. L., Chester, F. M., Kronenberg, A. K., & Chester, J. S., 2003. Subcritical compaction and yielding of granular quartz sand, **377**, 357–381.

Kepic, A. & Rosid, M., 2004. Enhancing the seismoelectric method via a virtual shot gather, *SEG Technical Program Expanded Abstracts*.

Knight, R. & Nolen-Hoeksema, R., 1990. A laboratory study of the dependence of elastic wave velocities on pore scale fluid distribution, *Geophys. Res. Lett.*, (17), 1529–1532.

Long, L. T. & Rivers, W. K., 1975. Field measurement of the electroseismic response, *Geophysics*, **40**, 233–245.

Lorne, B., Perrier, F., & Avouac, J.-P., 1999. Streaming potential measurements. 1. properties of the electrical double layer from crushed rock samples, *J. Geophys. Res.*, **104**(B8), 17.857–17.877.

Lorne, B., Perrier, F., & Avouac, J.-P., 1999. Streaming potential measurements. 2. relationship between electrical and hydraulic flow patterns from rocks samples during deformations, *J. Geophys. Res.*, **104**(B8), 17.857–17.877.

Martner, S. T. & Sparks, N. R., 1959. The electroseismic effect, *Geophysics*, **24**(2), 297–308.

Masson, Y. J., Pride, S. R., & Nihei, K. T., 2006. Finite difference modeling of biot's poroelastic equations at seismic frequencies, *J. Geophys. Res.*, **111**.

Mikhailenko, B. G. & Soboleva, O. N., 1997. Mathematical modeling of seismomagnetic effects arising in the seismic wave motion in the earth's constant magnetic field., *Appl. Math. Lett.*, **10**, 47–51.

Mironov, S. A., Parkhomenko, E. I., & Chernyak, G. Y., 1994. Seismoelectric effect in rocks containing gas or fluid hydrocarbon (english translation), *Physics of the solid earth*, **29**(11).

Murphy, W., Reischer, A., & Hsu, K., 1993. Modulus decomposition of compressionnal and shear velocities in sand bodies, *Geophysics*, **58**, 227–239.

Overbeek, J. T. G., 1952. Electrochemistry of the double layer., *Colloid Science, Irreversible Systems, edited by H. R. Kruyt, Elsevier*, **1**, 115–193.

Packard, R. G., 1953. Streaming potentials across capillaries for sinusoidal pressure, *J. Chem. Phys*, **1**(21), 303–307.

Pain, C., Saunders, J. H., Worthington, M. H., Singer, J. M., Stuart-Bruges, C. W., Mason, G., & Goddard., A., 2005. A mixed finite-element method for solving the poroelastic biot equations with electrokinetic coupling, *Geophys. J. Int.*, **160**, 592–608.

Parkhomenko, I. & Tsze-San, C., 1964. A study of the influence of moisture on the magnitude of the seismoelectric effect in sedimentary rocks by a laboratory method, *Bull. (Izv.) Acad. Sci., USSR, Geophys. Ser.*, pp. 115–118.

Pengra, D. B., Li, S. X., & Wong, P.-Z., 1999. Determination of rock properties by low frequency ac electrokinetics, *J. Geophys. Res.*, **104**(B12), 29.485–29.508.

Pozzi, J.-P. & Jouniaux, L., 1994. Electrical effects of fluid circulation in sediments and seismic prediction, *C.R. Acad. Sci. Paris, serie II*, **318**(1), 73–77.

Pride, S., 1994. Governing equations for the coupled electromagnetics and acoustics of porous media, *Physical Review B*, **50**, 15678–15695.

Pride, S. & Haartsen, M. W., 1996. Electroseismic wave properties, *J. Acoust. Soc. Am.*, **100**, 1301–1315.

Pride, S. R. & Berryman, J. G., 1998. Connecting theory to experiment in poroelasticity, *J. Mech. Phys. Solids*, **46**, 719–747.

Reppert, P. M., Morgan, F. D., Lesmes, D. P., & Jouniaux, L., 2001. Frequency-dependent streaming potentials, *Journal of Colloid and Interface Science*, (234), 194–203.

Russell, R. D., Butler, K. E., Kepic, A. W., & Maxwell, M., 1997. Seismoelectric exploration., *The Leading Edge*, pp. 1611–1615.

Saunders, J. H., Jackson, M. D., & Pain, C. C., 2006. A new numerical model of electrokinetic potential response during hydrocarbon recovery, *Geophys. Res. Lett.*, **33**.

Singer, B. S. & Fainberg, E. B., 1999. Modelling of electromagnetic fields in thin heterogeneous layers with application to field generation by volcanoes - theory and example, *Geophys. J. Int.*, **138**, 125–145.

Singer, J., J.Saunders, Holloway, L., Stoll, J., C.Pain, Stuart-Bruges, W., & Mason, G., 2005. Electrokinetic logging has the potential to measure the permeability, *Society of Petrophysicists and Well Log Analysts, 46th Annual Logging Symposium*.

Strahser, M. H., Rabbel, W., & Schildknecht, F., 2007. Polarisation and slowness of seismoelectric signals: a case study, *Near Surface Geophysics*, **5**, 97–114.

Thompson, A., Hornbostel, S., Burns, J., Murray, T., Raschke, R., Wride, J., McCammon, P., Sumner, J., Haake, G., Bixby, M., Ross, W., White, B., Zhou, M., & Peczak, P., 2005. Field tests of electroseismic hydrocarbon detection, *SEG Technical Program Expanded Abstracts*.

Thompson, A. H. & Gist, G. A., 1993. Geophysical applications of electrokinetic conversion, *The Leading Edge*, **12**, 1169–1173.

Thompson, R. R., 1936. The seismic-electric effect., *Geophysics*, **1**(3), 327–335.

Waysand, G., Bloyet, D., Bongiraux, J.-P., Collar, J.-I., Dolabdjian, C., & Thiec, P. L., 1999. First characterization of the ultra-shielded chamber in the low-noise underground laboratory (lsbb) of rustrel pays d'apt, *Workshop on Low Temperature Devices (LDT8), August 1999-Nuclear instrumentation and Methods in Physics Research*, (A444), 336–339.

Zhu, Z. & Toksöz, M. N., 2003. Crosshole seismoelectric measurements in borehole models with fractures, *Geophysics*, **68**(5), 1519–1524.

Zhu, Z. & Toksöz, M. N., 2005. Seismoelectric and seismomagnetic measurements in fractured borehole models, *Geophysics*, **70**(4), F45–F51.

Zhu, Z., Haartsen, M. W., & Toksöz, M. N., 1999. Experimental studies of electrokinetic conversions in fluid-saturated borehole models., *Geophysics*, **64**, 1349–1356.

Zhu, Z., Haartsen, M. W., & Toksöz, M. N., 2000. Experimental studies of seismoelectric conversions in fluid-saturated porous media., *J. Geophys. Res.*, **105**, 28,055–28,064.

A Pride's theory for seismo-electromagnetic couplings

A.1 Mechanical and transport macroscopic equations

The Biot's theory is the correct general model governing poroelastic response (Pride & Berryman, 1998; Pain et al., 2005; Masson et al., 2006). Poroelastic response allows for the coupled interactions between the elastic deformation of a porous solid and the fluid flow and fluid accumulation in the same material. The Pride's theory for the seismo-electromagnetic couplings is based on the connexion of the Biot's and Maxwell's equations via electrokinetic couplings. This theory is therefore suitable for the fluid flow induced by seismic wave. Pride (1994) obtained macroscopic equations governing mechanical motion, charge transport and electromagnetism laws characterizing the full wave propagation field. All notations used in this section are explicited in appendix C. The mechanical equations are obtained *via* a generalized Biot's law taking into account the boundary conditions at the pore scale:

$$\nabla \cdot \tau_{\mathbf{B}} = -\omega^2 \left(\rho \mathbf{u_s} + \rho_f \mathbf{w}\right) \tag{17}$$

$$\tau_{\mathbf{B}} = \left(K_G \nabla \cdot \mathbf{u_s} + C \nabla \cdot \mathbf{w}\right) \mathbf{I} + G \left(\nabla \mathbf{u_s} + \nabla \mathbf{u_s}^T - \frac{2}{3} \nabla \cdot \mathbf{u_s} \mathbf{I}\right) \tag{18}$$

$$-p = C \nabla \cdot \mathbf{u_s} + M \nabla \cdot \mathbf{w} \tag{19}$$

where τ_B is the stress tensor, $\mathbf{I}$ is the identity matrix, $\mathbf{u_s}$ is the displacement of the solid, and $\mathbf{w}$ is the average volume filtration. And K_G, C, M and Δ are poroelastic constants defined by:

$$K_G = \frac{K_{fr} + \phi K_f + (1+\phi) K_s \Delta}{1+\Delta} \tag{20}$$

$$C = \frac{K_f + K_s \Delta}{1+\Delta} \tag{21}$$

$$M = \frac{K_f}{\phi(1+\Delta)} \tag{22}$$

$$\Delta = \frac{K_f}{\phi K_s^2}\left[(1-\phi)K_s - K_{fr}\right] \tag{23}$$

The frame bulk modulus K_{fr} is the reverse of the compressibility, itself being a measure of the volumetric strain resulting from an applied change in pressure (Hart & Wang, 1995).

In section 2 the equations (1) and (2) refere to complex dynamic parameters such as electrokinetic coupling $L(\omega)$, permeability $k(\omega)$ and effective conductivity $\sigma(\omega)$:

$$L(\omega) = L_0\left[1 - i\frac{\omega}{\omega_c}\frac{m}{4}\left(1-2\frac{d}{\Lambda}\right)^2\left(1 - i^{3/2}d\sqrt{\frac{\omega\rho_f}{\eta}}\right)^2\right]^{-\frac{1}{2}} \tag{24}$$

where the static electrokinetic coupling is given by:

$$L_0 = -\frac{\phi}{\alpha_\infty}\frac{\varepsilon_{rf}\,\zeta}{\eta}\left(1-2\frac{d}{\Lambda}\right) \tag{25}$$

where m and Λ are geometrical parameters of the pores given in table C. The critical angular frequency ω_c separates the viscous and inertial flow domains and is defined by:

$$\omega_c = \frac{\phi}{\alpha_\infty k_0}\frac{\eta}{\rho_f} \tag{26}$$

Assuming that the d/Λ term is negligible, L_0 parameter can be expressed versus electrokinetic coupling C_{ek} from electrofiltration measurements (Guichet et al., 2003). Then:

$$L_0 \;=\; -\frac{\phi}{\alpha_\infty}\,C_{ek}\,\sigma_f \;=\; -C_{ek}\,\sigma_r \tag{27}$$

Expression of the effective conductivity of the material introduces surface conduction effects due to electrofiltration (C_{em}) and electro-osmotic (C_{os}) effects:

$$\sigma(\omega) = \frac{\phi\,\sigma_f}{\alpha_\infty}\left[1 + 2\frac{C_{em} + C_{os}(\omega)}{\sigma_f\Lambda}\right] \tag{28}$$

At last, the dynamic permeabilty of the porous media (Johnson et al., 1987) depends on the observed frequency, especially for very high frequencies:

$$k(\omega) = k_0 \left[\sqrt{1 - i\frac{\omega}{\omega_c}\frac{4}{m}} - i\frac{\omega}{\omega_c} \right]^{-1} \tag{29}$$

A.2 Phase velocities of body waves

The phase velocities analysis used in this paper is based on the formulation of Pride & Haartsen (1996) in the low frequency domain. This approach has been developed for seismoelectric studies, but in the case $L(\omega) = 0$ the phase velocities are equivalent to the Biot's results (1956). Slowness are expressed in the case of plane longitudinal and transverse waves:

For the fast P-waves:

$$2s_{Pf}^2 = \gamma - \sqrt{\gamma^2 - \frac{4\tilde{\rho}\rho}{MH - C^2}\left(\frac{\rho_t}{\rho} + \frac{\tilde{\rho}L(\omega)^2}{\tilde{\varepsilon}}\right)} \tag{30}$$

For the slow P-waves:

$$2s_{Ps}^2 = \gamma + \sqrt{\gamma^2 - \frac{4\tilde{\rho}\rho}{MH - C^2}\left(\frac{\rho_t}{\rho} + \frac{\tilde{\rho}L(\omega)^2}{\tilde{\varepsilon}}\right)} \tag{31}$$

where

$$\gamma = \frac{\rho M + \tilde{\rho}H(1 + \rho\frac{L(\omega)^2}{\tilde{\varepsilon}}) - 2\rho_f C}{MH - C^2} \tag{32}$$

For the S waves:

$$2s_S^2 = \frac{\rho_t}{G} + \mu_0\tilde{\varepsilon}\left(1 + \frac{\tilde{\rho}L(\omega)^2}{\tilde{\varepsilon}}\right) + \sqrt{\left[\frac{\rho_t}{G} - \mu_0\tilde{\varepsilon}\left(1 + \frac{\tilde{\rho}L(\omega)^2}{\tilde{\varepsilon}}\right)\right]^2 - 4\mu_0\frac{\rho_f^2 L(\omega)^2}{G}} \tag{33}$$

where $H = K_G + 4G$ is an elastic modulus, ρ_t the complex density and $\tilde{\rho}$ the effective density given by:

$$\rho_t = \rho - \frac{\rho_f^2}{\tilde{\rho}} \tag{34}$$

$$\tilde{\rho} = \frac{i}{\omega}\frac{\eta}{k(\omega)} \tag{35}$$

Attenuation effects of the Biot's theory are described by the imaginary part of the effective density $\tilde{\rho}$. In this expression $\tilde{\varepsilon}$ corresponds to the effective permittivity introducing conduction and electro-osmotic dissipation:

$$\tilde{\varepsilon} = \varepsilon_0\varepsilon_{rT} + \frac{i}{\omega}\sigma(\omega) - \tilde{\rho}(\omega)L^2(\omega) \tag{36}$$

B Seismo-electromagnetic fields in the porous cylindrical sample

Similarly to Hu & Wang (2000) study for a fluid-filled borehole, we consider an axisymetric porous system under vertical seismic excitation generating P-SV waves. According to Pride & Haartsen (1996), four different propagation modes should be taken into account: fast and slow P waves (P_f and P_s) as longitudinal modes and S and electromagnetic (em) waves as transverse modes. Nevertheless, we neglect electromagnetic modes generating electroosmotic displacements in the absence of significant source.

B.1 Seismomagnetic coupling from extensional modes

The total displacement $\mathbf{u}$ can be expressed in the (i_r, i_θ, i_z) coordinate system by:

$$\mathbf{u_e} = A_{P_f}\,\nabla\Phi_{P_f} \;+\; A_{P_s}\,\nabla\Phi_{P_s} \;+\; A_S\,\nabla\times(\Gamma_S\,i_\theta) \tag{37}$$

where Φ_{P_f} and Φ_{P_s} are scalar potentials and Γ_S a vector potential satisfiying the Helmholtz decomposition with wavenumbers $l_j = \omega\, s_j$. In the case of the vertical seismic source, the potentials can be expressed by:

$$\begin{cases} \Phi_{P_f} = I_0(\eta_{P_f}\, r)\; e^{ik_e z} \qquad \text{and} \qquad \Phi_{P_s} = I_0(\eta_{P_s}\, r)\; e^{ik_e z} \\ \Gamma_S = I_1(\eta_S\, r)\; e^{ik_e z} \end{cases} \tag{38}$$

where I_i are the modified Bessel's function of order i and η_j ($j = P_f, P_s$ or S) are related to the axial wavenumber k_e of extensional waves (in the vertical direction z) by the relation:

$$\eta_j \;=\; \sqrt{k_e^2 - l_j^2} \tag{39}$$

where $l_j = \omega s_j$ are the radial wavenumbers of each mode. Then, components of the displacement $\mathbf{u}$ can be calculated:

$$\mathbf{u_e} = \begin{bmatrix} A_{P_f}\,\eta_{P_f}\,I_1(\eta_{P_f}\,r) \;+ A_{P_s}\,\eta_{P_s}\,I_1(\eta_{P_s}\,r) \;- i\,k_e\;A_s\,I_1(\eta_S\,r) \\ 0 \\ i\,k_e\;A_{P_f}\,I_0(\eta_{P_f}\,r) \;\;+\; i\,k_e\,A_{P_s}\,I_0(\eta_{P_s}\,r) \;+ A_s\,\eta_s\,I_0(\eta_S\,r) \end{bmatrix}_{(\,r,\theta,\,z\,)} e^{ik_e z} \tag{40}$$

According to Pride & Haartsen (1996), the seismoelectric field can be deduced *via* appropriate coefficients β_j for each propagation mode:

$$\mathbf{E_e} = \begin{bmatrix} \beta_{P_f} A_{P_f}\,\eta_{P_f}\,I_1(\eta_{P_f}\,r) \;+ \beta_{P_s} A_{P_s}\,\eta_{P_s}\,I_1(\eta_{P_s}\,r) \;- i\,k_e\;\beta_S A_s\,I_1(\eta_S\,r) \\ 0 \\ i\,k_e\,\beta_{P_f}\;A_{P_f}\,I_0(\eta_{P_f}\,r) \;\;+\; i\,k_e\,\beta_{P_s} A_{P_s}\,\mathbf{I_0}(\eta_{P_s}\,r) \;+ \beta_s A_s\,\eta_s\,I_0(\eta_S\,r) \end{bmatrix}_{(\,r,\theta,\,z\,)} e^{ik_e z} \tag{41}$$

where coefficients β_j are given by:

$$\beta_j = \begin{cases} \frac{i\,\omega L\tilde{\rho}}{\tilde{\varepsilon}}\left(\frac{Hs_j^2-\rho}{Cs_j^2-\rho_f}\right) & for \qquad j = P_f \text{ or } P_s \\ \\ -i\omega\mu\tilde{\rho}L\frac{G}{\rho_f}\left(\frac{s_j^2-\frac{\rho}{G}}{s_j^2-\mu\tilde{\varepsilon}}\right) & \text{for} \qquad j = S \end{cases} \tag{42}$$

where ρ, C and M formation parameters are given by equations 21 and 22. Then, the seismomagnetic field $\mathbf{H}$ can be deduced from classical Maxwell's equation:

$$\mathbf{H} = -\frac{i}{\omega\;\mu}\;(\nabla \times \mathbf{E}) \tag{43}$$

where μ is the magnetic permeability of the free space. Combined with equation 6, this equation leads to:

$$\mathbf{H_e} = \begin{bmatrix} 0 \\ \frac{1}{i\mu}\,\omega\,s_S^2\,A_S\,\beta_S\,I_1(\eta_S\,r) \\ 0 \end{bmatrix}_{(\,r,\theta,\,z\,)} e^{ik_e z} \tag{44}$$

By comparison with equation 40 we get:

$$H_{e,\theta} = \frac{1}{i\mu}\frac{\beta_S\,s_S^2}{k_e}\;\frac{du_{s,r}}{dt} \tag{45}$$

This equation shows that the seismomagnetic field associated to extensional waves is proportional to the grain velocity of S waves *via* the dynamic variables β_S, s_S^2 and k_e.

B.2 Seismomagnetic coupling from S waves

On the other hand, seismomagnetic coupling can be generated by pure S waves. Using the same procedure, we can obtain the expressions of seismoelectric and magnetic fields

$$\mathbf{E_s} = \begin{bmatrix} -i\, k_s\, I_1(\eta_S\, r) \\ 0 \\ \eta_s\, I_0(\eta_S\, r) \end{bmatrix}_{(r,\theta,z)} A_S\, \beta_S\, e^{ik_s z} \tag{46}$$

and

$$\mathbf{H_s} = \begin{bmatrix} 0 \\ \frac{1}{i\mu}\, \omega\, s_S^2\, A_S\, \beta_S\, I_1(\eta_S\, r) \\ 0 \end{bmatrix}_{(r,\theta,z)} e^{ik_s z} \tag{47}$$

leading to

$$H_{s,\theta} = \frac{1}{i\mu} \frac{\beta_S\, s_S^2}{k_s} \frac{du_{s,r}}{dt} \tag{48}$$

This expression shows that the seismomagnetic field is proportional to the grain velocity of s waves similarly to extensional mode (note the difference of coefficient with k_s instead of k_e).

B.3 Low frequency approximation

As suggested by Garambois & Dietrich (2001), the low frequency approximation leads to a significantly simpler form of equation 48. Using the same procedure (not detailed here) we use the zero frequency value of the S wave slowness:

$$s_S^2 = \frac{\rho_t}{G} \tag{49}$$

Using the zero frequency electrokinetic coupling L_0, the β_S coefficient can be expressed by:

$$\beta_S = i\omega\mu L_0 \frac{G\,\rho_f}{\rho_t} \tag{50}$$

Leading to the relation:

$$H_{s,\theta} = \omega L_0 \frac{\rho_f}{k_s}\,\frac{du_{s,r}}{dt} = H_\theta = L_0 \rho_f \sqrt{\frac{G}{\rho}}\,\frac{du_{s,r}}{dt} \tag{51}$$

Using the definition of the electrokinetic coupling:

$$L_0 = -\frac{\phi}{\alpha_\infty}\frac{\epsilon_0\,\kappa_f\,\zeta}{\eta} \tag{52}$$

we get:

$$H_{s,\theta} = -\frac{\phi}{\alpha_\infty}\frac{\epsilon_0\,\kappa_f\,\zeta}{\eta}\rho_f \sqrt{\frac{G}{\rho}}\,\frac{du_{s,r}}{dt} \tag{53}$$

Using the same procedure, we get the expression of the seismomagnetic field associated to extensional modes:

$$H_{e,\theta} = -\frac{\phi}{\alpha_\infty}\frac{\epsilon_0\,\kappa_f\,\zeta}{\eta}\rho_f \sqrt{\frac{E}{\rho}}\,\frac{du_{s,r}}{dt} \tag{54}$$

where E is the Young's modulus of the sample defined by equation 10. The low frequency approximation shows that the seismomagnetic field is proportional to the radial grain velocity associated to S waves. The transfert function depends on the origin of the seismic propagation (S or extensional waves), *via* the phase velocities $\sqrt{E/\rho}$ and $\sqrt{G/\rho}$. A simple comparison of the transfert functions from equations 48 and 53 leads to the conclusion that the error from low frequency approximation is lower than 2% in the range of 100 to 3000 Hz.

C Notations

[Table 3 about here.]

List of Figures

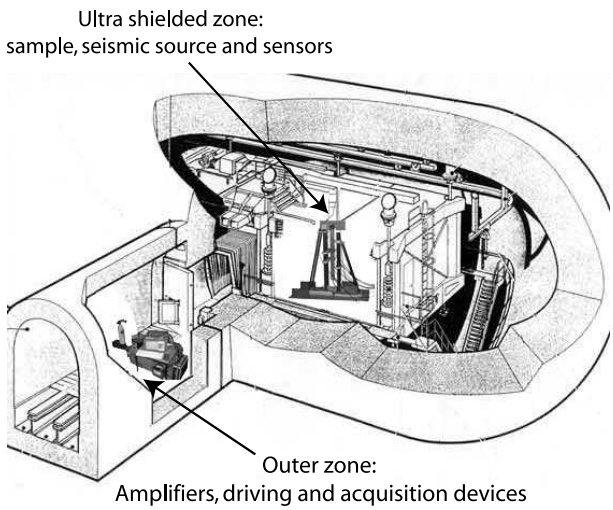

Figure 1: Sensitive part of the experiment (sample and magnetometers) is located within the ultrashielded chamber of the laboratory whereas devices generating electromagnetic disturbances are located outside. The ambient magnetic noise is lower than 2 $fT/\sqrt{Hz}$ above 10 Hz within the chamber *(adapted from http://lsbb.unice.fr)*

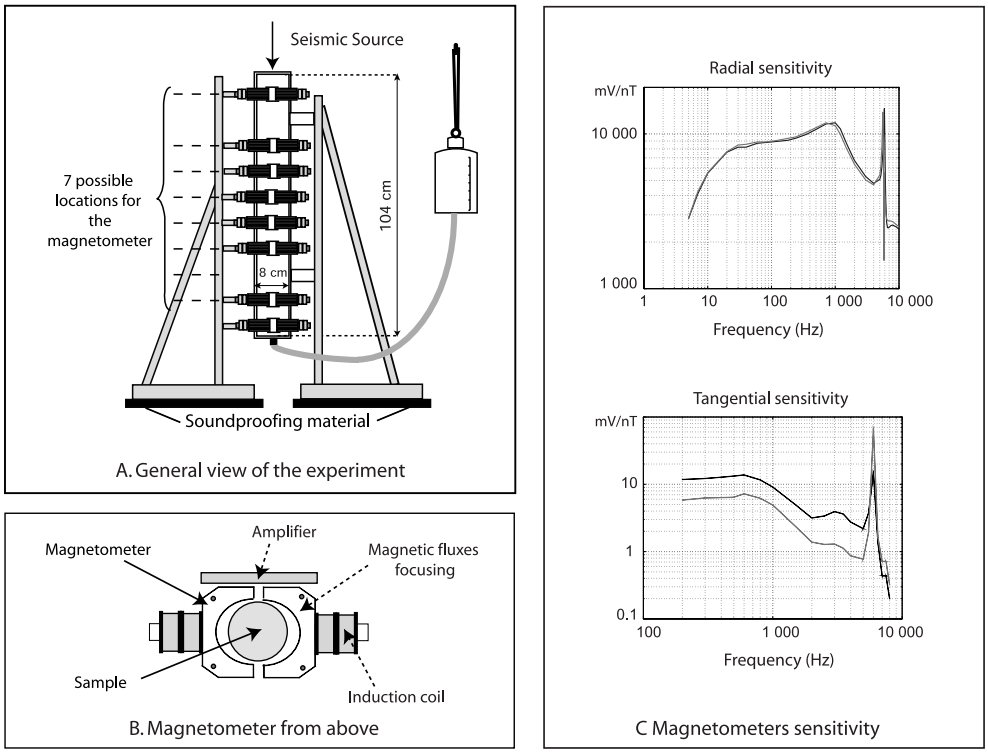

Figure 2: A. The magnetometers and the Plexyglas column are fixed on two different stands; B. The induction magnetometers consist in two focusing cores and induction coils; C. Radial sensitivity of magnetometers is around 10 V/nT and **azimuthal** sensitivity is around 10 mV/nT (grey and black lines are respectively attributed to lower and upper magnetometer

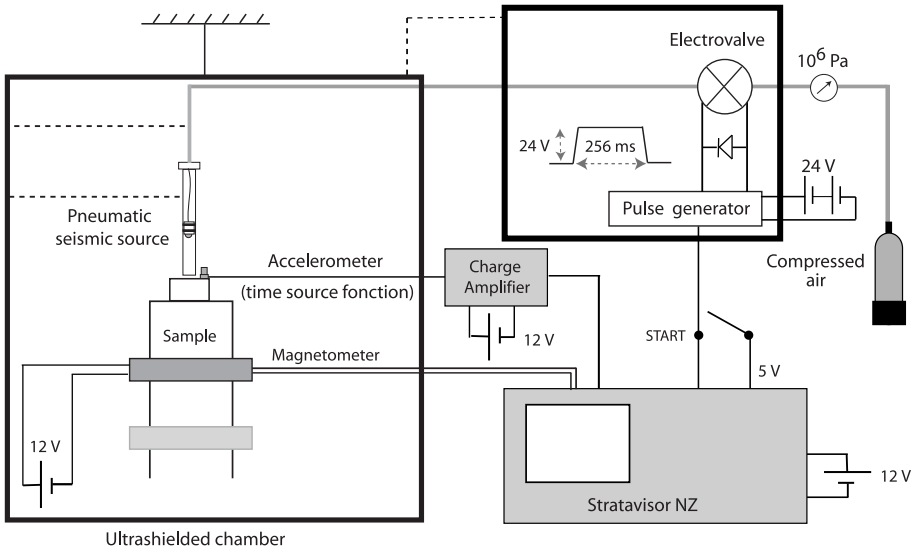

Figure 3: General scheme of the experiment showing devices located within and outside the underground shielded chamber

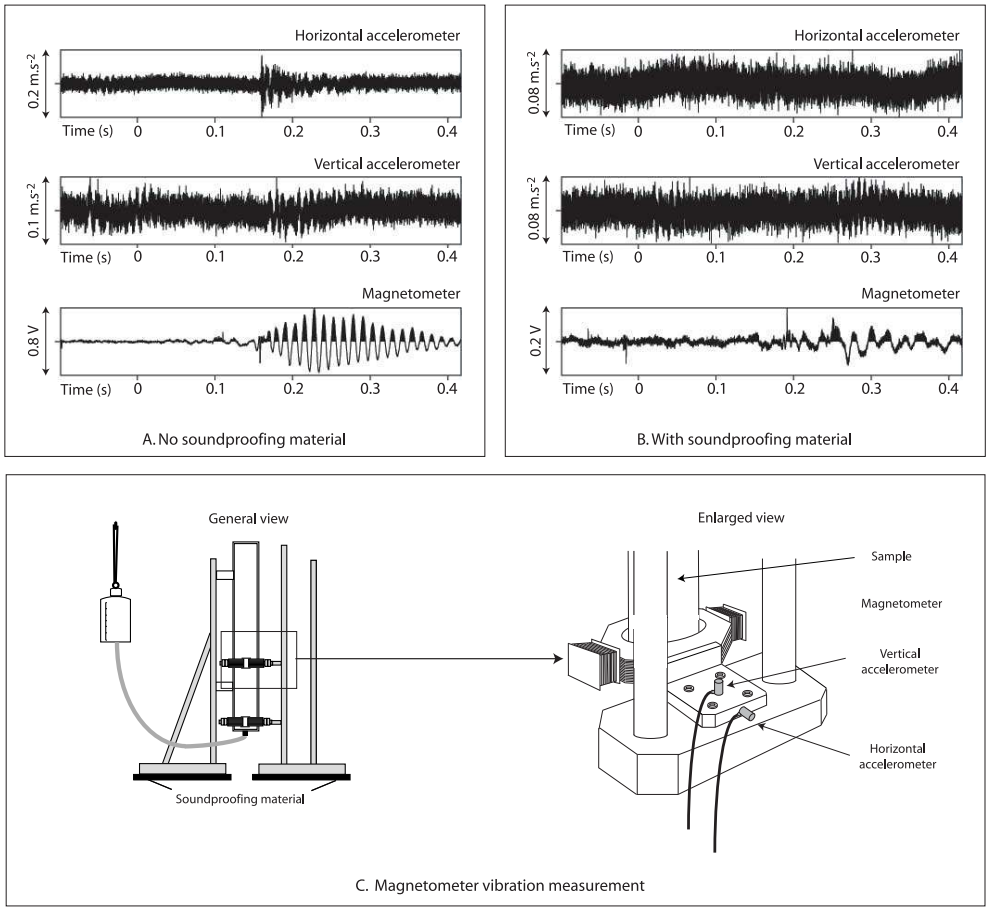

Figure 4: Disturbances due to weak vibrations of the magnetometers occuring after one shot, normalized for a 1 m.s^{-2} seismic source. This simple test clearly shows that the magnetometer's vibrations are very weak and barely measurable but generate some strong transient magnetic signals (part A). This phenomena can be strongly attenuated by introducing a soundproofing protection on the floor (part B)

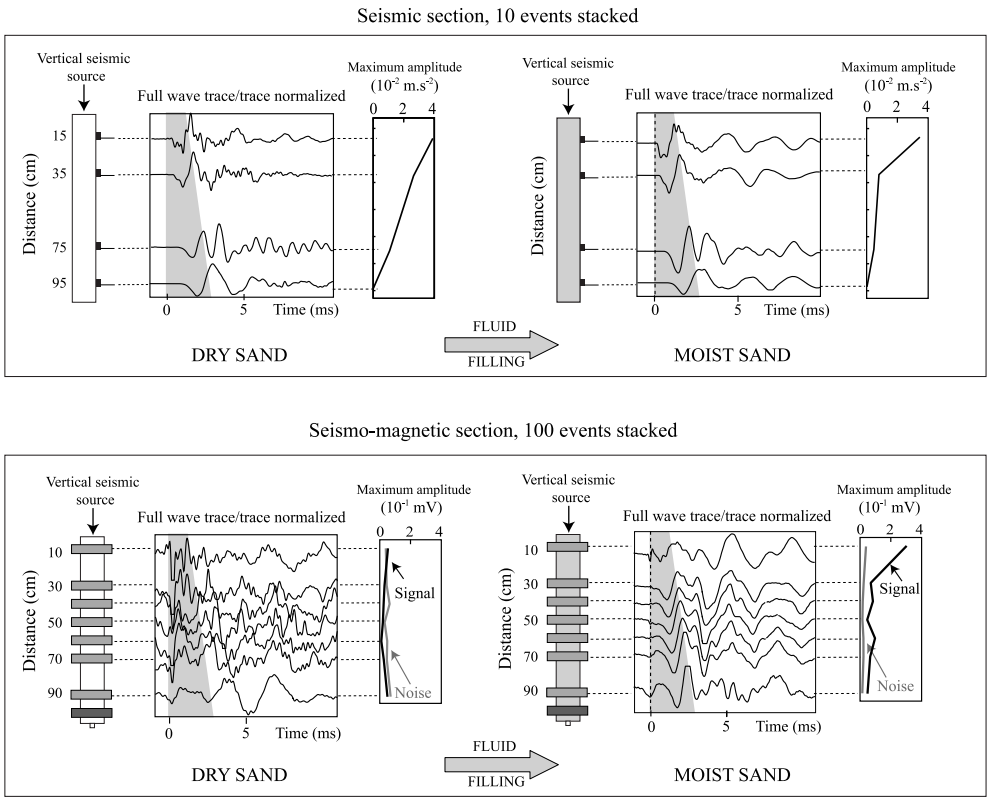

Figure 5: Comparison of seismic and seismo-magnetic measurements on dry and moist compacted sand showing the evidence of coherent magnetic arrival in the moist sand. The seismo-magnetic signal is referenced to the lower magnetometer.

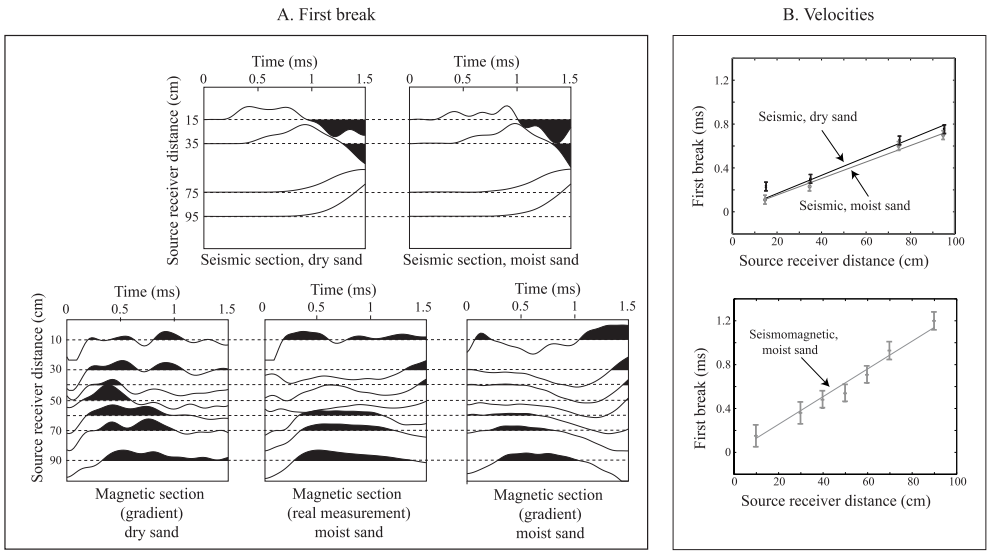

Figure 6: Zoom on first break of the seismic and seismo-magnetic measurements (trace/trace normalised). The seismo-magnetic gradient representation improves the velocity resolution by partly substracting the disturbance occuring around $t = 0\ s$. Apparent velocities in moist sand are measured to be $1328 \pm 94\, m.s^{-1}$ for seismic wave and $791 \pm 80\, m.s^{-1}$ for the seismo-magnetic wave.

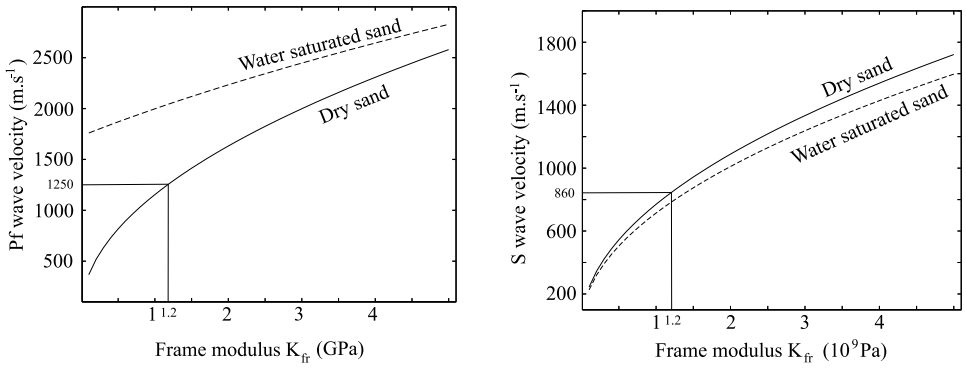

Figure 7: Computation of the seismic velocities from versus frame modulus K_{fr} in the dry and water saturated cases (Pride & Haartsen, 1996) . Considering the measured P_f velocity (1250 $m.s^{-1}$), the corresponding frame modulus of the sand can be estimated to 1.2 GPa. The calculated S wave velocity, deduced from this K_{fr} value, is near 860 $m.s^{-1}$.

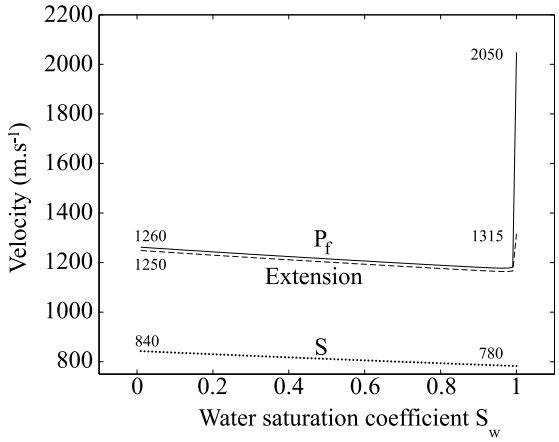

Figure 8: Comparison of the phase velocities of P_f, extension and S waves versus saturation coefficient. The P and extensional waves can not be distinguished by velocity measurements

List of Tables

Measured parameters

ϕ	k_0 (m^2)	σ_f $(S.m^{-1})$	C_{ek} from Guichet et al. (2003) $(V.Pa^{-1})$
0.3	$5.8\ 10^{-12}$	$3.1\ 10^{-3}$	$-6545\ 10^{-9}$

Assumed parameters

	α	ρ_f $(kg.m^{-3})$	ρ_s (silica) $(kg.m^{-3})$	η $(Pa.s)$	K_s (Pa)	K_f (Pa)
Water	3	1000	2650	0.001	$36\ 10^9$	$2.22\ 10^9$
Air	3	1.2		$18\ 10^{-6}$		$0.15\ 10^6$

Table 1: Values of the parameters used for computations. Electrokinetic coupling measured by Guichet et al. (2003) on Fontainebleau sand was converted to the measured fluid conductivity.

Source Type	Source-receiver distance (m)	Measured acceleration (g) ($m.s^{-2}$)
Terrestrial Air Gun	15	0.5
Explosives (200 g)	7.5	96
Sledgehammer blow	10	0.05
Vibroseis (P-waves)	5	3 (vertical)
Vibroseis (S-waves)	5	4 (horizontal)

Table 2: Measured acceleration versus source-receiver distance for different seismic sources (personnal data). The terrestrial air gun (Vesdun en Berry, France) consists in an air gun placed in an artificial basin

α_∞	Tortuosity	
ε_0	Dielectric constant of the free space	$\varepsilon_0 = 8,85418782.10^{-12}$
ε_{rT}, ε_{rf}, ε_{rs}	Dielectric constants (total, fluid and solid)	
$\tilde{\varepsilon}$	Effective permittivity	*cf* equation 36
η	Fluid viscosity	
k_0	Measured permeability	$5.8\ 10^{-12}$ m^2
$k(\omega)$	Dynamic permeability	*cf* equation 29
Λ	Pore geometry parameter	$\Lambda = \sqrt{\frac{\kappa_0\ m\ \alpha_\infty}{\phi}}$
ρ_f, ρ_s and ρ	Fluid, solid and total bulk density	$\rho = \phi\rho_f + (1-\phi)\rho_s$
ρ_t	Complex density	*cf* equation 34
$\tilde{\rho}$	Effective density	*cf* equation 35
σ_f	Electrical conductivity of the fluid	$3.1\ mS/m$
σ_s	Electrical conductivity of the grains	
$\sigma(\omega)$	Effective conductivity	*cf* equation 28
τ_B	General stress tensor	$\tau_B = \phi\tau_f + (1-\phi)\tau_s$
τ_f and τ_s	Fluid and solid stress tensor	
ϕ	Porosity	
ω	Pulsation	
ω_c	Critical frequency	$\omega_c = \frac{\phi}{\alpha_\infty\kappa_0}\frac{\eta}{\rho_f}$
ζ	Zeta potential	
C_{ek}	Electrofiltration coupling	
d	Debye length	$d = \frac{3\cdot 10^{-10}}{\sqrt{C_0}}$
G	Frame shear modulus	
E and H	Seismo-electric and seismo-magnetic fields	
H	Elastic constant	$H = K_G + 4G$
K_G	Gassman's modulus	$K_G = \frac{K_{fr}+\phi K_f+(1+\phi)K_s\Delta}{1+\Delta}$
K_{fr}, K_f and K_s	Frame, fluid and grain bulk moduli	
$L(\omega)$	Dynamic electrokinetic coupling	*cf* equation 3
L_0	Static electrokinetic coupling	*cf* equation 4
m	Geometrical parameter of the pores	$2 \leq m \leq 8$
p	Pore pressure	
S_w	Saturation coefficient	
$\mathbf{u}_s$, $\mathbf{u}_f$	Displacement of the solid and the fluid	
$\mathbf{u}$	Total displacement	
$\mathbf{w}$	Volume average filtration (fluid flow)	$\mathbf{w} = \phi(\mathbf{u_s} - \mathbf{u_f})$